Monthly Notices of the ROYAL ASTRONOMICAL SOCIETY

MNRAS **499,** 2042–2050 (2020) doi:10.1093/mnras/staa2949
Advance Access publication 2020 September 25

Early science with the LMT: molecular torus in UGC 5101

I. Cruz-González [1]★ A. I. Gómez-Ruiz,[2]★ A. Caldú-Primo,[1] E. Benítez [1]
J. M. Rodríguez-Espinosa [3,4] Y. Krongold [1] I. Aretxaga,[5] R. Snell,[6] O. González-Martin,[7]
C. A. Negrete,[8] G. Narayanan,[6] D. H. Hughes,[5] M. S. Yun,[6] G. G. Fazio,[9] V. Chavushyan,[5] D. Hiriart,[10]
E. Jiménez-Bailón,[10] M. Herrera-Endoqui,[10] M. Martínez-Paredes[11] and J. J. González[1]

[1]*Instituto de Astronomía, Universidad Nacional Autónoma de México, Apdo. Postal 70-264, CDMX 04510, Mexico*
[2]*CONACYT-Instituto Nacional de Astrofísica Óptica y Electrónica, Luis E. Erro 1, 72840 Tonantzintla, Puebla, Mexico*
[3]*Instituto de Astrofísica de Canarias, C/ Vía Láctea, s/n, E38205 La Laguna (Tenerife), Spain*
[4]*Departamento de Astrofísica, Universidad de La Laguna, E38206 La Laguna, Spain*
[5]*Instituto Nacional de Astrofísica Óptica y Electrónica, Luis E. Erro 1, 72840 Tonantzintla, Puebla, Mexico*
[6]*Department of Astronomy, University of Massachusetts, Amherst, MA 01003, USA*
[7]*Instituto de Radioastronomía y Astrofísica, Universidad Nacional Autónoma de México, Apdo. Postal 3-72, Morelia 58089, Mexico*
[8]*CONACYT-Instituto de Astronomía, Universidad Nacional Autónoma de México, Apdo. Postal 70-264, CDMX 04510, Mexico*
[9]*Harvard-Smithsonian Center for Astrophysics, 60 Garden St, Cambridge, MA 02138, USA*
[10]*Instituto de Astronomía, Universidad Nacional Autónoma de México, Apdo. Postal 877, Ensenada BC 22800, Mexico*
[11]*Korea Astronomy and Space Science Institute 776, Daedeokdae-ro, Yuseong-gu, Daejeon 34055, Republic of Korea*

Accepted 2020 September 4. Received 2020 September 4; in original form 2020 May 1

ABSTRACT

As part of the Early Science Large Millimeter Telescope projects, we report the detection of nine double-peaked molecular lines, produced by a rotating molecular torus, in the ultraluminous infrared galaxies (ULIRG) – Compton-thick active galactic nuclei (AGN) galaxy UGC 5101. The double-peaked lines we report correspond to molecular transitions of HCN, HCO^+, HNC, N_2H^+, CS, $C^{18}O$, ^{13}CO, and two CN lines; plus the detection of C_2H that is a blend of six lines. The redshift search receiver spectra covers the 73–113 GHz frequency window. Low- and high-density gas tracers of the torus have different implied rotational velocities, with a rotational velocity of 149 ± 3 km s^{-1} for the low-density ones ($C^{18}O$, ^{13}CO) and 174 ± 3 km s^{-1} for high-density tracers (HCN, HCO^+, HNC, N_2H^+, CS, and CN). In UGC 5101, we find that the ratio of integrated intensities of HCN to ^{13}CO to be unusually large, probably indicating that the gas in the torus is very dense. Both the column densities and abundances are consistent with values found in AGN, starburst, and ULIRG galaxies. The observed abundance ratios cannot discriminate between X-ray and UV-field-dominated regions.

Key words: galaxies: active – galaxies: individual: UGC 5101 – galaxies: ISM – galaxies: nuclei.

1 INTRODUCTION

Since the review work of Young & Scoville (1991), surveys of molecular gas emitted at millimetre frequencies, in large samples of galaxies, have grown from tenths (Gao & Solomon 2004a,b, and references therein) to hundreds of sources (e.g. Saintonge et al. 2011a,b, 2017). Observations of molecular gas mass tracers as ^{12}CO and ^{13}CO and the active star formation tracers associated with high-density gas such as HCN, CS, and HCO^+ (cf. Genzel 1992) of nearby galaxies are valuable to study the physical conditions of their interstellar medium (ISM).

Studies of the ISM of starbursts, quiescent spirals, and irregular galaxies show strong differences (e.g. Genzel et al. 2012; Scoville 2013). Molecular gas during the merging process of galaxies plays a crucial role in the geometrical relocation of molecular clouds. From a disc distribution, in disc galaxies, the molecular gas concentrates in the central kpc regions of ultraluminous infrared galaxies (ULIRG; $L_{8-1000\,\mu m} > 10^{12}$ L$_\odot$) and in active galactic nuclei (AGN; e.g. Scoville 1991; Downes & Solomon 1998), with densities comparable to the stellar densities of elliptical galaxies. Spectra of molecular transitions show that the gas is concentrated in rotating nuclear discs or rings with typical radii of 300–800 pc.

N-body simulations of galaxy mergers (e.g. Barnes & Hernquist 1992; Hopkins, Quataert & Murray 2012) have shown that gas-rich galaxy mergers are capable of triggering large starbursts and AGN activity, which are both observed in most ULIRGs (e.g. Veilleux 2012). Most major mergers involve an initial close approach followed by a second one that leads to coalescence, whereas the infalling gas disc towards the nuclear region restores rotational support at a radius of a few hundred parsecs (e.g. Hopkins, Quataert & Murray 2011). Mergers may lead to compaction, in which the star-forming gas migrates inwards and triggers a central starburst (e.g. Barnes & Hernquist 1992; Hopkins et al. 2011, 2012). Follow-up studies done in ULIRGs have shown that these objects are invariably associated with major disc galaxy mergers, supported by evidence of double-nuclei and nuclear activity (e.g. Joseph & Wright 1985; Melnick & Mirabel 1990; Soifer et al. 2000). Moreover, their inner nuclear

★ E-mail: irene@astro.unam.mx (IC-G); aigomez@inaoep.mx (AIG-R)

regions (few hundreds pc) harbour very large masses of gas and dust (see review by Lonsdale, Farrah & Smith 2006). Galaxy mergers drive gas inflows that can trigger the AGN (e.g. Surace et al. 1998; Treister et al. 2012). Dense gas in the nuclear region provides material that enables the growth of the supermassive black hole (e.g. Hopkins & Hernquist 2009; Komossa, Baker & Liu 2016) by triggering AGN activity and major starbursts.

UGC 5101 (CGCG 289-011; IRAS 09320+6134; MCG +10-14-025; SDSS J093551.59+612111.3) has a single very red nucleus harbored by a galaxy that shows disturbed morphology suggestive of galaxy interaction. It has been classified as a late-stage merger by Veilleux, Kim & Sanders (2002). At $z = 0.03937$ ($D_L = 174.8$ Mpc; 1 arcsec = 784 pc; Wright 2006), it is one of the brightest infrared sources in the local Universe ($\log L_{\rm FIR}/L_{\odot} = 11.96$; Sanders et al. 2003). It is one of the so-called ULIRG that is undergoing a strong circumnuclear starburst. Optically, UGC 5101 has been classified as an intermediate Seyfert (Sy) 1.5 galaxy by Sanders et al. (1988); as a Sy 1 by Véron-Cetty & Véron (2010); as a LINER by Veilleux et al. (1995), and as a Sy 2 by Yuan, Kewley & Sanders (2010). Nevertheless, the Baldwin–Peterson–Terlevich diagnostic diagrams presented by Wild et al. (2011) and Malkan et al. (2017) favour a Sy1.5/LINER classification. Furthermore, high-resolution MIR spectra show characteristic polycyclic aromatic hydrocarbon (PAH) features associated with starbursts (Martínez-Paredes et al. 2015). All these results indicate an intermediate luminosity AGN buried in a strong starburst.

The radio brightness temperature (T_b) of UGC 5101 is found to be high in Condon et al. (1990) and Condon, Frayer & Broderick (1991). *VLA* observations at 1.4 GHz, complemented with 8.44 GHz A-configuration data, show that the slightly resolved nucleus is an AGN source (at 8.44 GHz has $\log T_b = 4.56$) with a size of 0.14 arcsec × 0.11 arcsec. At 1.6 GHz, the radio nucleus of UGC 5101 has a $T_b > 10^7$ K and is resolved with the VLBI (Lonsdale et al. 2003), together with a possible jet of extent 0.13 arcsec × 0.11 arcsec with five knots. They suggest that the AGN is responsible for at least 10 per cent of the total radio flux at 1.6 GHz.

Wilson et al. (2008) present Submillimeter Array *(SMA)* CO J = 3-2 data cubes and 800 μm continuum maps that trace, respectively, the molecular gas and dust of a sample of ULIRGs. They include the galaxy UGC 5101 and Iono et al. (2009) measured an angular source size of extent 1.1 arcsec × 0.8 arcsec for the CO(3-2) disc.

Spectroscopy in the 3 mm band has been reported by Imanishi et al. (2009) with the *Nobeyama* telescope, while Costagliola et al. (2011) and Privon et al. (2015), among others, present 3 mm spectra with the *IRAM* telescope. This literature shows that J = 1→0 transitions of HCN, HCO^+, HNC, and ^{12}CO lines are detected.

Mid-IR high angular resolution (subarcsec) studies (Martínez-Paredes et al. 2015; Alonso-Herrero et al. 2016) found that 20 per cent of the emission in the Si2 band (8.7 μm) comes from an unresolved nuclear source smaller than 300 pc in radius. Additionally, Martínez-Paredes et al. (2015) found that the *CanariCam/GTC spectrum*, obtained within a nuclear region of ∼300 pc, can be separated into a power law (due to AGN emission) and a strong starburst component. They also showed that the unresolved emission at the near-IR *NICMOS/HST* image, plus the mid-IR *CanariCam/GTC*, and the starburst-subtracted *CanariCam/GTC* spectrum can constrain models of the CLUMPY dusty torus proposed by Nenkova et al. (2008a,b), which predict a dusty torus with a radial size of ∼35 pc (∼0.027 arcsec at the distance of UGC 5101).

Hard X-ray (2–10 keV) studies using data from Chandra and *XMM–Newton* satellites have revealed the presence of the Fe–Kα emission line with an equivalent width of ∼400 eV (Imanishi et al. 2003; González-Martín et al. 2009). These results, together with the low ratios of L_x(2–10 keV)/$L_{\rm IR}$ and L_x(2–10 keV)/$L_{[\rm O\,III]}$ measured for this galaxy, suggest the presence of a Compton-thick AGN (Imanishi et al. 2003; Ptak et al. 2003; González-Martín et al. 2009). XMM data indicate an obscured, but luminous, hard X-ray source with L_x(2–10 keV) ∼ 5×10^{42} erg s^{-1}, and ratio L_x(2–10 keV)/$L_{\rm IR}$ ∼0.002 suggestive of a buried AGN (e.g. Imanishi et al. 2003).

Recently, Oda et al. (2017) used all available X-ray data between 0.25 and 100 keV (*Swift/Burst Alert Telescope, NuSTAR, Suzaku, XMM–Newton*, and *Chandra*) plus analytical and numerical torus models to reproduce the X-ray spectrum of UGC 5101. They detect a barely Compton-thick AGN with a line-of-sight (LOS) column density N_H(LOS) ∼ 1.3×10^{24} cm^{-2}, which is at the limit between Compton-thin and Compton-thick sources. Additionally, they found a weak intrinsic X-ray absorption N_H(*host*) ∼ 1.3×10^{21} cm^{-2}, and suggest that the AGN in UGC 5101 is surrounded by two obscuring components: a Compton-thick one located close to the equatorial plane of the torus, and a Compton-thin one associated to the torus-hole region. The size measured using SED modelling (∼35 pc; Martínez-Paredes et al. 2015) could then be related to the Compton-thick region.

UGC 5101 offers an ideal scenario to study star formation activity and its possible interplay or connection to the AGN. Therefore, as part of the Early Science Large Millimeter Telescope (LMT) projects, we report observations with the redshift search receiver (RSR) of the ULIRG Compton-thick AGN galaxy UGC 5101. We aim to probe its molecular gas emission by studying different molecular emission lines across the whole 3 mm band and their associated densities. Section 2 describes the observations with the RSR/LMT and opacity conditions. Section 3 covers the data reduction methodology and shows the spectra, while Section 4 presents the analysis. We summarize our results and discussions in Section 5.

Throughout our work, we adopt a cosmology where $H_0 = 69.6$ km s^{-1} Mpc^{-1}, $\Omega_m = 0.286$, and $\Omega_\lambda = 0.714$ (Bennett et al. 2014).

2 OBSERVATIONS

Observations of UGC 5101 were obtained between November 2014 and March 2017 with the RSR on the LMT Alfonso Serrano, hereon RSR/LMT, in its early science phase. In this early phase, the LMT operated with a 32-m active surface, which then resulted in a half-power beam of width 26 arcsec at the centre of the 3 mm band. Observing conditions at the Volcán Sierra Negra site were very good most of the time, with system temperature, $T_{\rm sys}$, in the range of 85–110 K. Observations were centred on the coordinates of the galaxy nucleus, with the OFF beam 39 arcsec apart. Pointing accuracy was found to be better than 2 arcsec. The total ON source integration time on UGC 5101 was 9 h.

The RSR is an autocorrelator spectrometer with a monolithic microwave-integrated circuit system that receives signals over four pixels, simultaneously covering the frequency range 73–GHz at $\Delta\nu =$ 31 MHz spectral resolution, which corresponds to ∼100 km s^{-1}at 90 GHz (Erickson et al. 2007). Hence, across the whole 3 mm band the velocity resolution changes from 85 to 125 km s^{-1}. The RSR/LMT-32m has a spatial resolution or beam full width at half-maximum (which is frequency dependent, ranging from 31 to 20 arcsec, between 73 and 111 GHz).

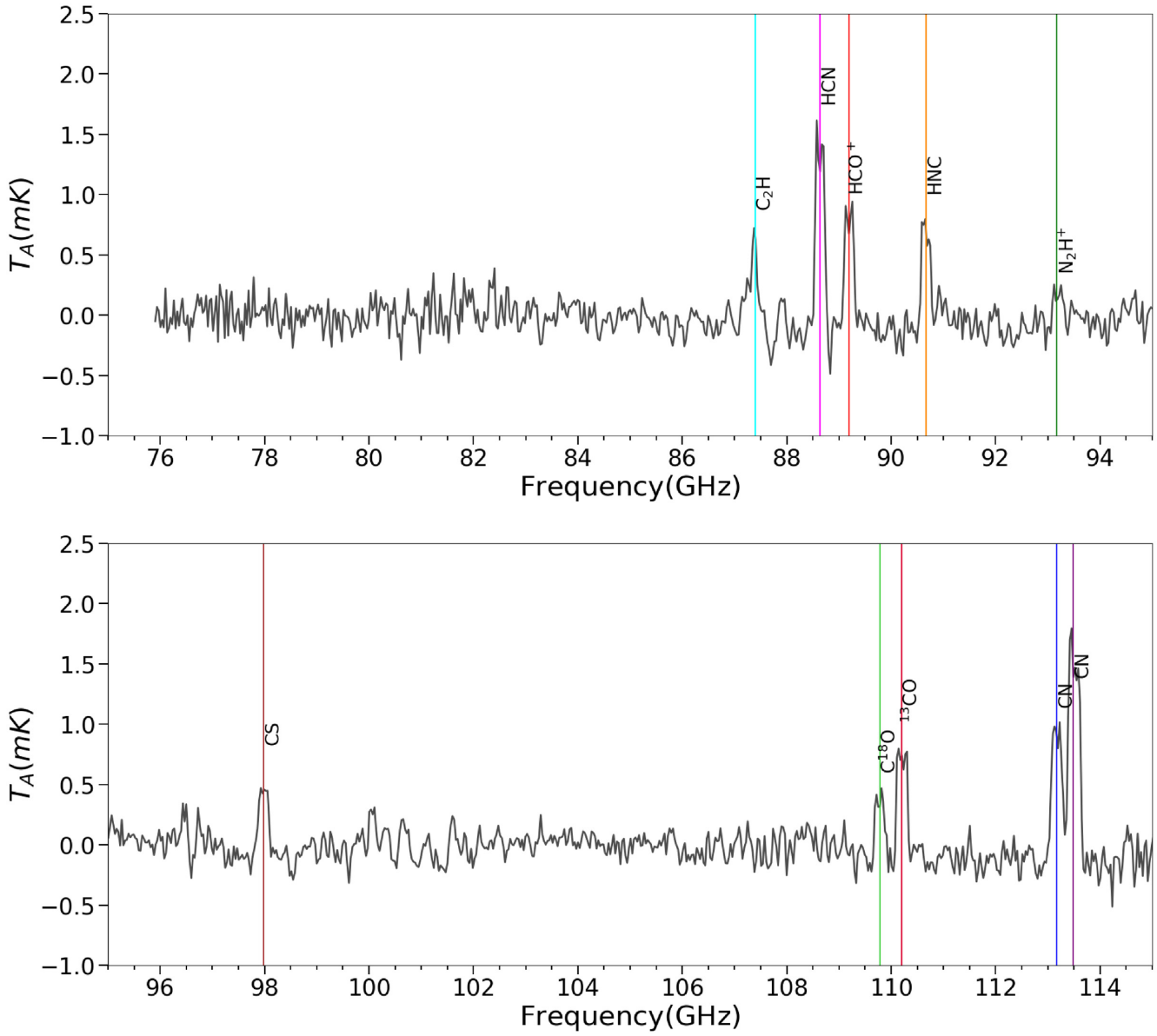

Figure 1. Redshift Search Receiver (RSR/LMT) spectra from 75 to 115 GHz of UGC 5101. The observed frequency has been corrected for the optical redshift and so rest frequencies are shown. The vertical colour lines show likely frequencies of some molecular transitions. Note that the detected transitions with a $S/N > 3$ shown in the top panel are C_2H, HCN, HCO^+, HNC, and N_2H^+, while the bottom panel shows detections of CS, $C^{18}O$, ^{13}CO, and two CN lines.

3 REDUCED SPECTRA

Autocorrelations, spectral co-adding, calibration, and baseline removal were carried out with the Data REduction and Analysis Methods in Python (Dreampy) software, developed by Gopal Narayanan for the RSR. After removing integrations with unstable bandpass, the remaining spectra are averaged weighted by the root mean square (RMS) noise in each individual spectrum. A simple linear baseline is removed in each spectral chassis that covers 6.5 GHz section of the total RSR bandwidth, after masking strong emission lines. To convert from antenna temperature (T_A) units to Jy, we used a conversion factor (Jy K^{-1}) of 6.4 for $\nu < 92$ GHz and 7.6 for $\nu >$ 92 GHz. To convert antenna temperature to main beam temperature, T_{MB}, we multiplied the spectrum by a factor that has the form 1.2 $\exp((\nu/170)^2)$, where ν is the sky frequency of the observed line. Such expression was obtained from calibration observations performed in 2017 January. Details of the RSR/LMT data reduction can be found in a number of articles, for example, see Snell et al. (2011), Lee et al. (2014), Yun et al. (2015), and Cybulski et al. (2016).

The RSR covers in the rest frame of UGC 5101, which is at a redshift of 0.0394, a frequency range of 76–115 GHz. The entire RSR spectrum is shown in Fig. 1. The *RMS* of the spectrum varies slightly across the frequency band, varying from 0.118 mK on the low-frequency end to 0.107 mK at the high-frequency end. A number of molecular spectral lines are clearly detected in this spectrum. Using a 3σ detection threshold on the integrated intensity of the line, we detected 10 spectral lines: C_2H at 87.40 GHz N = 1–0, which is a blend of six lines: J = 3/2-1/2 (F = 1-1, 2-1, 1-0) and J = 1/2-1/2 (F = 1-1, 0-1, 1-0); HCN(1-0), HCO^+(1-0), HNC(1-0), N_2H^+, CS(2–1), $C^{18}O$(1-0), and ^{13}CO(1-0) at 88.63, 89.19, 90.66, 93.17, 97.98, 109.78, and 110.20 GHz, respectively; and two transitions of CN at

Table 1. Molecular line transitions detected in UGC 5101.

Molecule	Transition	Frequency (GHz)	Beam (arcsec)	Peak intensity (mK)	Integrated flux (K km s^{-1})
(1)	(2)	(3)	(4)	(5)	(6)
C_2H^a	N = 1–0	87.284–87.447	25.2	1.31 ± 0.19	0.92 ± 0.08
HCN	$J = 1 \rightarrow 0$	88.631	24.8	2.76 ± 0.19	1.63 ± 0.07
HCO^+	$J = 1 \rightarrow 0$	89.189	24.7	1.71 ± 0.19	1.09 ± 0.06
HNC	$J = 1 \rightarrow 0$	90.663	24.3	1.47 ± 0.19	0.90 ± 0.07
N_2H^+	$J = 1 \rightarrow 0$	93.174	23.7	0.47 ± 0.19	0.22 ± 0.06
CS	$J = 2 \rightarrow 1$	97.980	22.5	0.79 ± 0.18	0.46 ± 0.06
$C^{18}O$	$J = 1 \rightarrow 0$	109.78	20.1	0.98 ± 0.20	0.42 ± 0.06
^{13}CO	$J = 1 \rightarrow 0$	110.20	20.0	1.55 ± 0.20	0.90 ± 0.06
CN	N = 1–0, $J = \frac{1}{2} \rightarrow \frac{1}{2}$	113.17	19.5	2.24 ± 0.21	1.33 ± 0.06
CN	N = 1–0, $J = \frac{3}{2} \rightarrow \frac{1}{2}$	113.49	19.4	3.73 ± 0.21	2.25 ± 0.06

Notes. Col. 3: Rest frequencies, obtained from the Splatalogue database: https://www.cv.nrao.edu/php/splat/.
Col. 4: Beam size at observed frequency.
Co. 5: Peak intensity in main beam temperature (T_{MB}) units.
Col. 6: Integrated flux.
[a]The molecular transition of C_2H N=1–0 is a blend of 6 lines: $J = \frac{3}{2} \rightarrow \frac{1}{2}$ (F = 1-1, 2-1, 1-0) $J = \frac{1}{2} \rightarrow \frac{1}{2}$ (F = 1-1, 0-1, 1-0).

113.17 and 113.49 GHz. The detected spectral lines are summarized in Table 1. Our spectrum included a part of the ^{12}CO line, however, since it lies on the edge of the spectrometer frequency range, it will not be used in our analysis. UGC 5101 was also observed by Costagliola et al. (2011) who found many of the lines we detected in UGC 5101 (positive detections of HCN, HCO^+, HNC, the two CN transitions and ^{12}CO). However, our spectrum has considerably better signal to noise, allowing us to detect in addition C_2H, N_2H^+, CS, $C^{18}O$, and ^{13}CO, and to examine the line profile shapes which was not possibly in their data.

The integrated intensity of each molecular line was found by integrating the spectrum over a frequency range of 341 MHz (11 spectral channels) centred on the frequency of each line. This frequency range corresponds to roughly a V_{LSR} range of -500 to $+500$ km s^{-1} for each line. For C_2H, we had to modify our method for computing the integrated intensity. The N = 1–0 C_2H feature at 87.35 GHz is a blend of the two spin-doublets (J = 3/2-1/2 and J = 1/2-1/2) and each doublet has additional hyperfine structure. For the J = 3/2-1/2 transition the frequency of the hyperfine components (F = 1-1, 2-1, and 1-0) range from 87.284 to 87.328 GHz, and for the J = 1/2-1/2 transition the hyperfine components (F = 1-1, 0-1, and 1-0) range from 87.402 to 87.447 GHz. Thus, these components are spread over the frequency interval of 163 MHz or slightly over five spectral channels. The observed line is noticeably broadened by this blending. Although other spectral lines have hyperfine components, such as HCN and N_2H^+, however, in these cases the components are spread only over a few MHz, much smaller than the spectrometer channel widths of 31 MHz, so they have no impact on the line profile. The integrated intensity for C_2H was found by integrating over 496 MHz, covering roughly the same velocity range as the other molecules for the C_2H components at the highest and lowest frequency. Lines and blends in which the integrated intensity was at least three times the estimate of the 1σ uncertainty are considered detections. The peak and integrated intensities for the 10 lines in main beam temperature units are given in Table 1.

4 ANALYSIS

Continuum regions were defined outside a window set by $v_0 \pm 500$ km s^{-1}, with v_0 the velocity corresponding to the central frequency of each line. The *RMS* was defined within the continuum regions.

The nine lines that make our signal-to-noise (S/N) cut ($S/N \geq 3$) are double peaked: HCN(1–0), HCO^+(1–0), HNC(1–0), N_2H^+, CS(2–1), $C^{18}O$(1–0), ^{13}CO(1–0), and the two CN transitions (1/2–1/2) and (3/2–1/2). In Fig. 2, the molecular emission of each line is presented individually. We note that since the emission of C_2H is a blend of six lines, it was not possible to study the line profile, so this blend will not be used in our line profile analysis.

In Fig. 3, the spectra of the nine detected molecular lines with double-peaked profiles are shown together. The double-peaked feature is most likely the result of a molecular rotating disc. In principle, self-absorption could also produce a double-peaked profile. However, the lines we observe span several hundreds of km s^{-1}, making it very unlikely to be explained by self-absorption.

For the analysis, a double-Gaussian fit was performed on each line. The rotation velocity (Table 2, column 2) was computed using the peak velocities of each of the fitted two-Gaussian components and dividing the result by 2. The corresponding error is computed with the parameter error estimation of the covariance matrix of the fit. Note that the errors in the rotation velocity are smaller that the velocity resolution of the 3 mm band of $\sim$100 km s^{-1}.

In order to further study this double-peaked feature, S/N was increased by splitting the lines in two groups and stacking them. The first group includes high density tracers (HCN, HCO^+,HNC, N_2H^+, CS, and the two CN lines) and the second group includes low-density tracers ($C^{18}O$ and ^{13}CO).

Before stacking, each individual line is centred at zero velocity by shifting it using the corresponding rest frequency obtained from the optical redshift. Each line is given a weight defined by their *S/N* ratio, using the line's peak intensity divided by the *RMS*. Finally, each spectrum is normalized by its peak intensity. A stacking of the spectra is performed for each group. For low-density tracers, in which case we only have two lines, the stacking error is taken as the value of the *RMS* at each point. For high-density tracers, the stacking errors were computed following Caldú-Primo et al. (2013): five random spectra were selected from the seven individual high-density tracers, allowing for repetition. Stacking of the resulting selection was then performed as before. This procedure was repeated 100 times and the error at each point is taken as the standard deviation for the 100 fits.

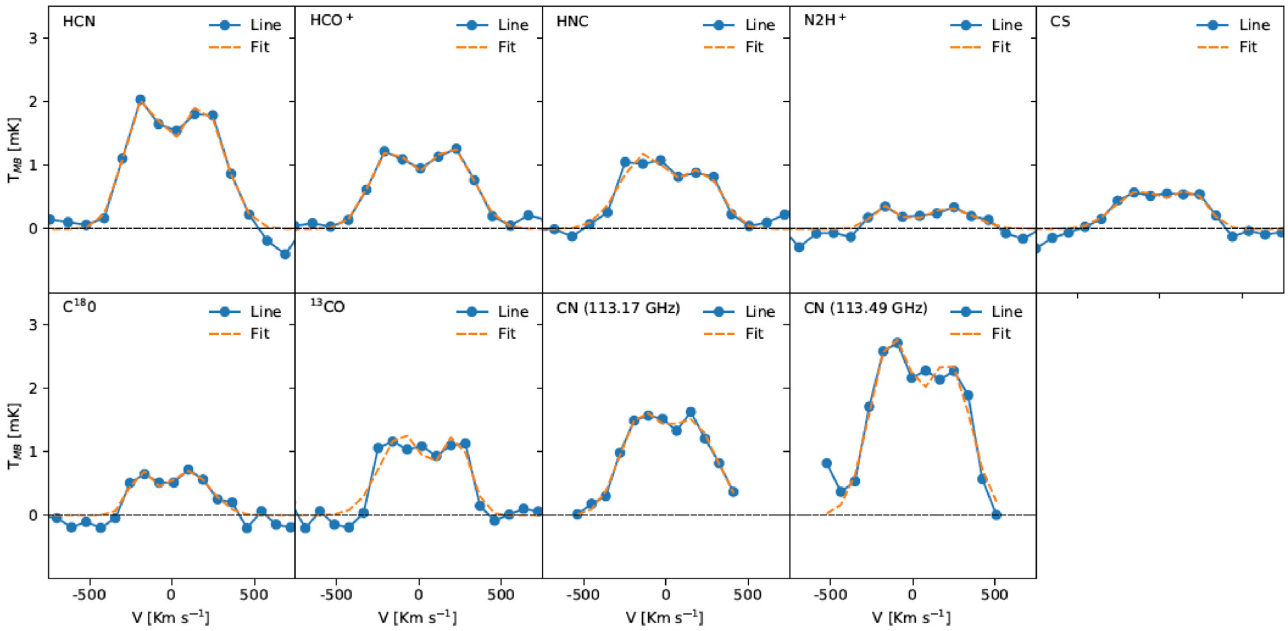

Figure 2. Double-peaked observed (blue) molecular lines of UGC5101 and their double-Gaussian fits (the orange-dashed line). From left to right the molecular lines are (top row) HCN, HCO^+, HNC, N_2H^+, and CS; (bottom row) $C^{18}O$, ^{13}CO, and the two CN transitions.

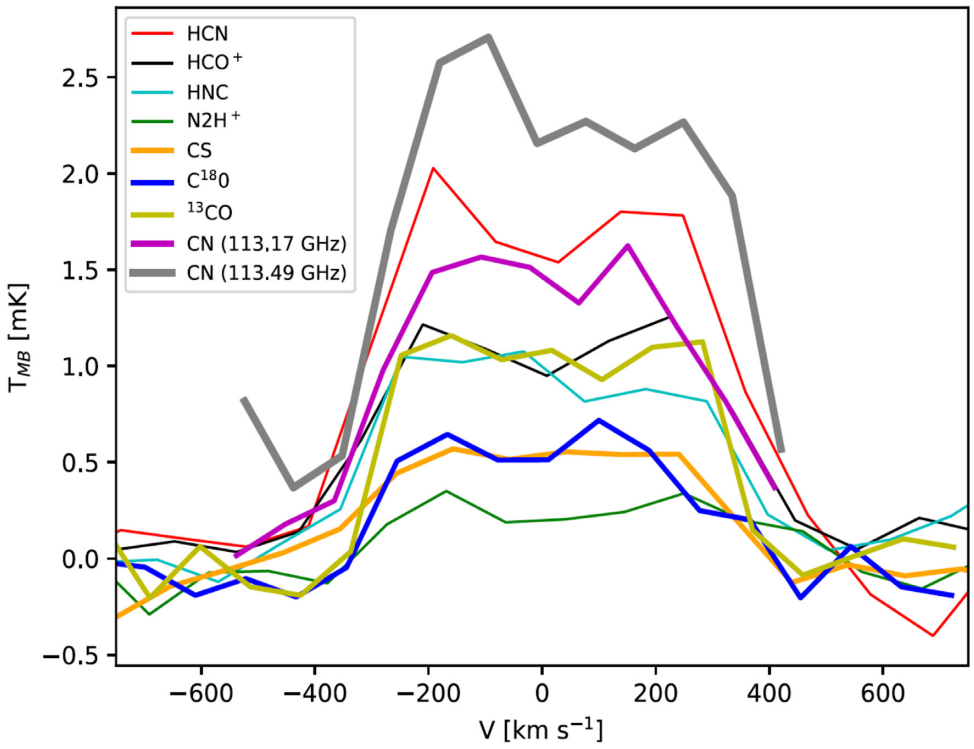

Figure 3. Observed overplotted spectra of nine molecular lines in the 3 mm spectrum of UGC 5101 showing a double-peaked profile.

After the stacking is done, a double-Gaussian fit is performed using Python's *curve_fit* procedure. The results are shown in Fig. 4 for high-density tracers and in Fig. 5 for low-density tracers.

The rotation velocity is measured as before, using the peak values of the two-Gaussian fit components. The error is computed by performing the fit 100 times as described before. The rotation velocity derived for the stacked spectra of the low-density tracers is $149 \pm 3\,\mathrm{km\,s^{-1}}$ and for the stacked spectra of high-density tracers it is $174 \pm 3\,\mathrm{km\,s^{-1}}$.

Finally, to determine the column density we need to make some assumptions and we have followed those made by Aladro et al. (2015), so we can make a direct comparison with their results. We assume that the level populations are in LTE and described by a rotational temperature of 10 K. However, before computing the column densities, we have corrected the integrated intensities

Table 2. Molecular line derived parameters.

Molecule	V_{rot} (km s^{-1})	N (cm^{-2})	$\frac{N}{N(C^{18}O)}$
(1)	(2)	(3)	(4)
C_2H	–	$(1.40 \pm 0.12) \times 10^{16}$	0.072 ± 0.011
HCN(1–0)	179 ± 24	$(2.24 \pm 0.09) \times 10^{15}$	0.011 ± 0.002
HCO^+(1–0)	185 ± 41	$(8.52 \pm 0.50) \times 10^{14}$	0.0044 ± 0.0006
HNC(1–0)	178 ± 71	$(1.06 \pm 0.08) \times 10^{15}$	0.0054 ± 0.00083
N_2H^+	194 ± 69	$(1.99 \pm 0.57) \times 10^{14}$	0.0010 ± 0.00032
CS	158 ± 103	$(1.72 \pm 0.16) \times 10^{15}$	0.009 ± 0.001
$C^{18}O$(1–0)	146 ± 48	$(1.95 \pm 0.26) \times 10^{17}$	1
^{13}CO(1–0)	163 ± 38	$(4.17 \pm 0.26) \times 10^{17}$	2.10 ± 0.31
CN($\frac{1}{2} - \frac{1}{2}$)	142 ± 72	$(7.64 \pm 0.31) \times 10^{15}$	0.0390 ± 0.0055
CN($\frac{3}{2} - \frac{1}{2}$)	176 ± 32	$(8.20 \pm 0.20) \times 10^{15}$	0.0420 ± 0.0057

Note. Col. 2: Rotation velocity. Col. 3: Column density. Col. 4: Abundance of each individual molecule compared to $C^{18}O$.

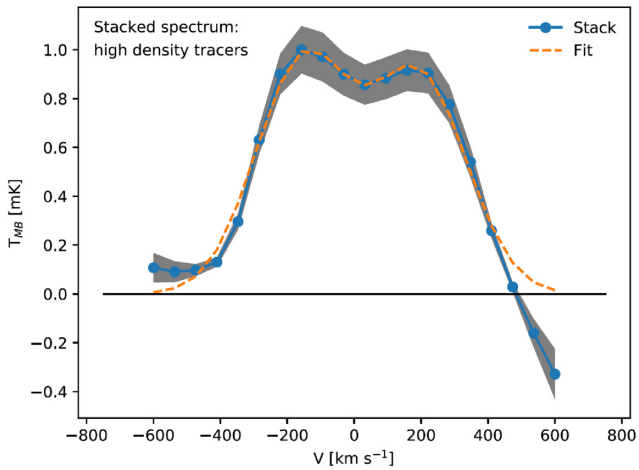

Figure 4. Stacked spectrum of the high-density tracers HCN, HCO^+, HNC, N_2H^+, CS, and the two CN lines. The blue solid lines with circles are data points; the fit is shown with the orange-dashed line. The shaded region shows the 1σ deviation from the bootstrap measurements.

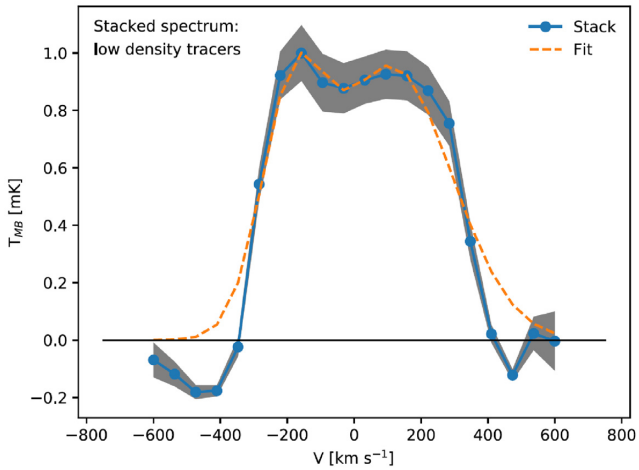

Figure 5. Stacked spectrum of the low-density tracers $C^{18}O$ and ^{13}CO. The blue solid lines with circles are data points; the fit is shown with the line. The shaded region shows the 1σ deviation from the bootstrap measurements.

of the lines given in Table 1 for the beam filling factor. Iono et al. (2009) measured an angular source size for UGC 5101 of 1.1 arcsec $\times$ 0.8 arcsec based on an interferometer map of the CO J = 3-2 line. We have assumed that the emission we observe comes from this same small region in UGC 5101 and correct accordingly by the beam filling factor. Even after correcting for this large beam dilution, the lines are all less than 1.5 K, and for a rotational temperature of 10 K, these lines would be optically thin, similar to what Aladro et al. found for the lines in their sample of galaxies. If the rotational temperature was larger, then the lines would have even smaller optical depths. Wilson et al. (2008) estimated that only about half of the total CO (3-2) line flux was coming from the regions mapped with the interferometer, thus some of the line emission we observe could be coming from a more extended region, and this would also lead to smaller optical depths for the lines we observe.

For some molecular species, we can test our modeling result that the lines are optically thin. Although we did not recover the entire ^{12}CO line, we know that the intensity of ^{12}CO is at least 20 times larger than ^{13}CO, indicating that both ^{13}CO and $C^{18}O$ are optically thin. We also can test the optical depth of the CN lines, the strongest line in our spectrum other than CO. If the CN lines are optically thin, the ratio of the spin doublet (the ratio of the J = 3/2-1/2 line to the J = 1/2-1/2 line) should be 2. The ratio we measure is consistent with the strongest of the spin doublet having at most a moderate optical depth. To be safe, we will use the CN column density derived from the weaker of the spin doublet lines. Since the other lines we observe are weaker, it is likely that they are all optically thin and consistent with our LTE models for a rotational temperature of 10 K. The column densities we compute for each molecular species are given in Table 2.

We note that increasing the rotational temperature to 30 K, which may be more appropriate for AGNs than star-forming region temperatures (e.g. Baan, Loenen & Spaans 2010), would roughly double the column densities presented in Table 2. However, if the same fraction of emission from the molecules we observe are in an extended component as was found for the CO J = 3-2 emission, then the column densities could be as much as a factor two smaller. However, these changes would have only a small effect on column density ratios that we will discuss later.

From the column densities, we also computed molecular abundances relative to $C^{18}O$. The column densities and relative abundances are reported in Table 2.

5 DISCUSSION

The RSR/LMT spectra in the 74–111 GHz band shows detected emission with $S/N > 3$ in 10 molecular transitions (see Table 1): C_2H, HCN, HCO^+, HNC, N_2H^+, CS, $C^{18}O$, ^{13}CO, and the two CN transitions. The most intense lines are the CN N = 1–0, J = $\frac{3}{2} \rightarrow \frac{1}{2}$ transition, followed by the HCN line and the CN N = 1–0, J = $\frac{1}{2} \rightarrow \frac{1}{2}$ transition (see Fig. 1 and peak intensity in Table 1).

The RSR/LMT spectra show double-peaked profiles in 9 of the 10 molecular transitions detected (see Table 2). Imanishi, Nakanishi & Kohno (2006) show that the nuclear spectra of UGC 5101 also shows a double-peaked profile for HCN(1–0), with a separation of 600 km s^{-1}, while for HCO^+(1–0) only a single peak is reported. The double-peaked profiles have been interpreted by most authors as produced by a molecular disc (e.g. Genzel et al. 1998; Imanishi et al. 2006; Wilson et al. 2008). Genzel et al. (1998) interferometric CO map report a starburst ring, where the molecular gas is also detected, with an inner and outer radius of 0.2 and 1.5 kpc, respectively. The molecular disc in UGC 5101 has been found with the SMA

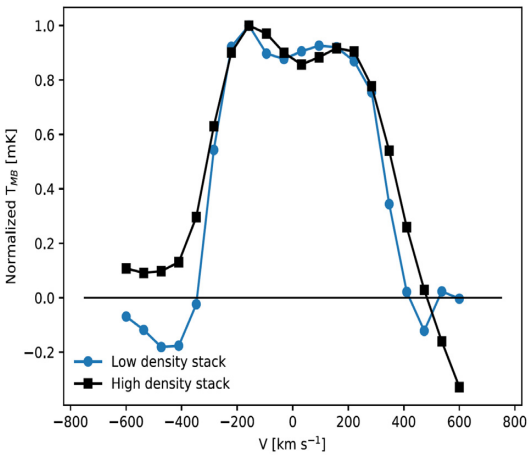

Figure 6. Inner out density gradient.

by (Wilson et al. 2008), both in CO(3–2) data cubes and 800 μm continuum. They also found $L_{CO} = 1.6 \times 10^9$ K km s^{-1} pc^2, $T_{dust} = 35.5$ K, $M_{dust} = 5.67 \pm 1.38 \times 10^7$ $M_\odot$, $M_{H_2} = 2.65 \pm 0.13 \times 10^9$ $M_\odot$ and a gas-to-dust ratio of 47 ± 11.

We can independently estimate the molecular gas mass based on our computed column density of ^{13}CO and a distance of 174 Mpc for UGC 5101. To derive the molecular gas mass we assume a ^{13}CO/H$_2$ abundance ratio of 2×10^{-6} (see discussion in Ripple et al. 2013). The molecular gas mass is estimated to be 2×10^9 $M_\odot$. This mass estimate agrees well with that estimated by Wilson et al. (2008), but is based on an assumed ^{13}CO abundance rather than on an assumed CO luminosity to gas mass conversion ratio.

As we mentioned above, the nucleus of the Compton-thick (Imanishi et al. 2003; Oda et al. 2017) AGN ULIRG UGC 5101, which globally has a star formation rate (SFR) of 93 $M_\odot$ yr^{-1} (Yun & Carilli 2002), is undergoing a strong nuclear starburst in a region of 392×755 pc^2 where the *SFR* is $\sim$3 $M_\odot$ yr^{-1} (Alonso-Herrero et al. 2016). The nucleus has an inner dusty and clumpy torus of $\sim$35 pc radius ($\sim$0.045 arcsec at the distance of UGC 5101; Martínez-Paredes et al. 2015). This compact inner torus is probably associated with the Compton-thick component found by Oda et al. (2017) with column density $N_H(LOS) \sim 1.3 \times 10^{24}$ cm^{-2}. This compact structure is surrounded by a molecular gas and dusty disc of $\sim$1.4–2 kpc extent (Wilson et al. 2008).

We have divided the molecular lines in two groups, with a first group consisting of high-density tracers (HCN, HCO$^+$, HNC, N_2H^+, CS, and the two CN lines) and a second group that includes low-density tracers (C^{18}O and ^{13}CO). As shown in the previous section, when lines are stacked by density, the rotational velocity results 149 ± 3 km s^{-1} for low-density tracers, while for high-density tracers it is somewhat larger, i.e. 174 ± 3 km s^{-1}. A comparison between the high-density and low-density stacked data is shown in Fig. 6. This small rotational velocity difference may be an indication of a density gradient. If we assume the gas is in near Keplerian rotation, then the inner regions which rotate faster have a higher density than the more slowly rotating outer regions.

5.1 Line intensity ratios

The strongest line in the spectrum of UGC 5101, other than CO, is the stronger of the spin-doublets of CN. CN is a photodissociation product of HCN and is often considered a photon-dominated regions (PDR) tracer (UV-irradiated regions). However, as noted by Aalto (2008), the presence of strong CN emission, and in this case more intense than the HCN line, may not distinguish between PDRs and XDRs, as large CN intensities are also expected in X-ray-irradiated regions (XDRs). In fact, in the samples of galaxies observed by Costagliola et al. (2011) and Aladro et al. (2015), the integrated intensity of the strongest of CN spin-doublet is usually stronger than HCN and their studies include a mix of starbursts and AGNs.

Baan et al. (2008) and Costagliola et al. (2011) examined the integrated intensity ratios for a large sample of galaxies. Both studies looked at line intensity ratios formed from combinations of HCN, HCO$^+$, and HNC, finding some interesting trends in these ratios. Both studies found an anticorrelation between the ratio of HCO$^+$/HCN versus HNC/HCO$^+$, while a correlation was found between the ratio of HNC/HCN versus HNC/HCO$^+$. Our data follow the trends found in these studies. Costagliola et al. found that galaxies with AGN tended to have a lower integrated intensity ratio of HCO$^+$/HCN. The ratio we measure in UGC 5101 is also relatively small, however, as Costagliola et al. notes, many of the LIRGs they observed also have small ratios and they suggest that the low ratio could be due to either low-density XDRs or high-density PDRs. In addition, Baan et al. noted that gas density may also play a role in the HCO$^+$/HCN ratio: smaller ratios may be produced by higher densities. Baan et al., based on PDR and XDR models of Meijerink & Spaans (2005) and Meijerink, Spaans & Israel (2006, 2007), predicted that the HNC/HCN intensity ratio should be greater than unity in XDR regions and less than unity in PDR regions. For UGC 5101 the observed ratio is 0.54, suggesting emission from a PDR. However, all but one of the galaxies in the Costagliola et al. study have ratios less than unity, despite the sample being a mix of starburst, AGNs, and LIRGs. It is not clear that these line ratios provide definitive evidence for the molecular gas environment.

What is most striking in UGC 5101 is the intensity of the high density tracers, such as HCN and HCO$^+$, relative to the isotopic lines of CO. For instance, the integrated intensity ratio HCN/^{13}CO is greater than 2. This is larger than most of the galaxies in the sample of Costagliola et al. (2011) and Aladro et al. (2015); only Arp 220 and Mrk 231 have comparable large ratios. Snell et al. (2011) suggested that this ratio was related to the average gas density: higher ratios implied larger gas densities. If correct, this suggests that the molecular gas density in the torus of UGC 5101 is high, larger than the gas densities typically found in the nuclear regions of galaxies. This result may not be a surprise, since UGC 5101 is a Compton-thick AGN.

5.2 Molecular abundances

The molecular abundances relative to C^{18}O are reported in Table 2, computed from the column densities estimated in previous sections.

Comparing our results with those presented for UGC 5101 by Costagliola et al. (2011), we see that the HNC/HCN abundance ratio is similar, and consistent within uncertainties between the two works. However, the HCN/HCO$^+$ and HNC/HCO$^+$ ratios are smaller in this work. This is a direct result of the higher data quality presented here, which allows us to have a much reliable measurement of the HCO$^+$ column density for this object. Considering the new values of HCN/HCO$^+$ and HNC/HCO$^+$, UGC 5101 cannot be considered as an extreme object in the Costagliola et al. (2011) sample (see their fig. 4), but rather an object with typical ratios.

In Table 3, we present a comparison of the abundance ratios in UGC 5101 with a subsample of the objects presented in Aladro et al. (2015). Both works have similar quality in their spectra, which makes a direct comparison straightforward. The sample by Aladro et al.

Table 3. Abundance ratios.

Ratio (1)	UGC 5101[a] (2)	M 82[b] (3)	M 83[b] (4)	NGC 7469[b] (5)	NGC 1068[b] (6)	Arp 220[b] (7)	Mrk 231[b] (8)
$C_2H/C^{18}O$	$(7.2 \pm 1.1) \times 10^{-2}$	1.4×10^{-1}	4.5×10^{-2}	1.6×10^{-1}	8.5×10^{-2}	3.5×10^{-2}	6.9×10^{-2}
$HCN/C^{18}O$	$(1.1 \pm 0.2) \times 10^{-2}$	1.1×10^{-2}	7.8×10^{-3}	1.6×10^{-2}	1.9×10^{-2}	7.4×10^{-3}	1.7×10^{-2}
$HNC/C^{18}O$	$(5.4 \pm 0.8) \times 10^{-3}$	4.4×10^{-3}	2.8×10^{-3}	6.6×10^{-3}	5.4×10^{-3}	5.2×10^{-3}	5.1×10^{-3}
$HCO^+/C^{18}O$	$(4.4 \pm 0.6) \times 10^{-3}$	1.0×10^{-2}	4.1×10^{-3}	1.1×10^{-2}	7.0×10^{-3}	1.8×10^{-3}	6.5×10^{-3}
$N_2H^+/C^{18}O$	$(1.0 \pm 0.3) \times 10^{-3}$	5.1×10^{-4}	5.9×10^{-4}	$\leq 1.3 \times 10^{-3}$	2.5×10^{-3}	9.5×10^{-4}	$\leq 1.1 \times 10^{-3}$
$^{13}CO/C^{18}O$	2.10 ± 0.31	5.0	5.2	5.6	3.6	1.1	1.1
$CN/C^{18}O$	$(3.7 \pm 2.0) \times 10^{-2}$	3.9×10^{-2}	2.9×10^{-2}	7.2×10^{-2}	5.3×10^{-2}	9.8×10^{-3}	3.7×10^{-2}
HCN/HCO^+	2.60 ± 0.19	1.1	1.9	1.4	2.7	4.1	2.6
HNC/HCN	0.47 ± 0.04	0.4	0.4	0.4	0.3	0.7	0.3
CN/HCN	3.40 ± 0.19	3.5	3.8	4.4	2.8	1.3	2.1
HCN/CS	1.30 ± 0.13	1.2	1.5	1.3	3.2	1.4	2.4

[a] This work. [b] From Aladro et al. (2015).

(2015) is composed of ULIRG, starburst, and AGN galaxies. We see that the abundance ratios observed in UGC 5101 are similar (within a factor ∼2) to the ratios observed in these type of galaxies. A noteworthy exception is the ^{13}CO / $C^{18}O$ ratio, which is much smaller than those for AGN and starbursts, and closer to the typical value ∼1 observed in ULIRGs, as Arp 220 and Mrk 231 in the Aladro et al. (2015) sample.

The abundances in UGC 5101 do not support an scenario where the chemistry is produced by only X-ray or UV-field-dominated regions, as similar ratios from PDRs and XDRs may be found in different conditions and at different column densities (e.g. see models by Meijerink & Spaans 2005). Most likely the abundances obtained for UGC 5101 molecular gas are due to the contribution of both XDRs and PDRs regions (Costagliola et al. 2011), which is consistent with the combined nature of our source being a Compton-thick AGN and a starburst galaxy in the ULIRG luminosity range.

As a final note, it is worth mentioning that if the gas kinetic temperature is 30 K instead of 10 K as assumed, the abundances estimates would double.

5.3 Final remarks

We conclude that UGC 5101 has a molecular gas torus with a Keplerian kinematic behaviour and a density gradient with increasing densities towards the central region. The line emission ratios are indicative of high densities in the torus, and the abundance ratios cannot discriminate between X-ray and UV-field-dominated regions.

ACKNOWLEDGEMENTS

We would like to thank the referee for carefully reading our manuscript and for giving such constructive comments that substantially helped in improving the quality of the paper. ICG, EB, JMRE, CAN, EJB, and MHE acknowledge support from DGAPA, UNAM grant IN113417. EB and ICG acknowledge support from DGAPA, UNAM grant IN113320. YK acknowledges support from DGAPA, UNAM grant IN106518 and DGAPA-PASPA 2016–2017. JMRE acknowledges support from the Spanish grants AYA2015-70498-C2-1, and AYA2017-84061-P de la AEI del Ministerio de Ciencia e Innovación, Spain. IA thanks support from CONACYT grant CB2016-281948. OGM thanks support from DGAPA, UNAM grant IA103118. The LMT acknowledges CONACYT funding to support the completion of the telescope construction and early science operations with the grants U0004-246083, U0004-259839, F0003-272050, M0037-279006, and F0003-281692, as well as support from the U.S. National Science Foundation via the University Radio Observatory program, the Instituto Nacional de Astrofísica, Óptica y Electrónica (INAOE) and the University of Massachusetts Amherst (UMASS). We also thank and greatly appreciate the support of the LMT's technical staff during the observations.

DATA AVAILABILITY

The data underlying this article will be shared on reasonable request to the corresponding author.

REFERENCES

Aalto S., 2008, Ap&SS, 313, 273
Aladro R. et al., 2015, A&A, 579, A101
Alonso-Herrero A. et al., 2016, MNRAS, 463, 2405
Baan W. A., Henkel C., Loenen A. F., Baudry A., Wiklind T., 2008, A&A, 477, 747
Baan W. A., Loenen E., Spaans M., 2010, Highlights Astron., 15, 411
Barnes J. E., Hernquist L., 1992, ARA&A, 30, 705
Bennett C. L., Larson D., Weiland J. L., Hinshaw G., 2014, ApJ, 794, 135
Caldú-Primo A., Schruba A., Walter F., Leroy A., Sandstrom K., de Blok W. J. G., Ianjamasimanana R., Mogotsi K. M., 2013, AJ, 146, 150
Condon J. J., Helou G., Sanders D. B., Soifer B. T., 1990, ApJS, 73, 359
Condon J. J., Frayer D. T., Broderick J. J., 1991, AJ, 101, 362
Costagliola F. et al., 2011, A&A, 528, A30
Cybulski R. et al., 2016, MNRAS, 459, 3287
Downes D., Solomon P. M., 1998, ApJ, 507, 615
Erickson N., Narayanan G., Goeller R., Grosslein R., 2007, in Baker A. J., Glenn J., Harris A. I., Mangum J. G., Yun M. S., eds, ASP Conf. Ser. Vol. 375, From Z-Machines to ALMA: (Sub)Millimeter Spectroscopy of Galaxies. Astron. Soc. Pac., San Fransisco, p. 71
Gao Y., Solomon P. M., 2004a, ApJS, 152, 63
Gao Y., Solomon P. M., 2004b, ApJ, 606, 271
Genzel R., 1992, in Burton W. B., Elmegreen B. G., Genzel R., Pfenniger D., Bartholdi P., eds, Saas-Fee Advanced Course 21: The Galactic Interstellar Medium, Springer Nature, Switzerland, p. 275
Genzel R. et al., 1998, ApJ, 498, 579
Genzel R. et al., 2012, ApJ, 746, 69
González-Martín O., Masegosa J., Márquez I., Guainazzi M., 2009, ApJ, 704, 1570
Hopkins P. F., Hernquist L., 2009, ApJ, 694, 599
Hopkins P. F., Quataert E., Murray N., 2011, MNRAS, 417, 950
Hopkins P. F., Quataert E., Murray N., 2012, MNRAS, 421, 3488
Imanishi M., Terashima Y., Anabuki N., Nakagawa T., 2003, ApJ, 596, L167
Imanishi M., Nakanishi K., Kohno K., 2006, AJ, 131, 2888
Imanishi M., Nakanishi K., Tamura Y., Peng C.-H., 2009, AJ, 137, 3581

Iono D. et al., 2009, ApJ, 695, 1537
Joseph R. D., Wright G. S., 1985, MNRAS, 214, 87
Komossa S., Baker J. G., Liu F. K., 2016, IAU Focus Meeting, 29B, 292
Lee C., Chung A., Yun M. S., Cybulski R., Narayanan G., Erickson N., 2014, MNRAS, 441, 1363
Lonsdale C. J., Lonsdale C. J., Smith H. E., Diamond P. J., 2003, ApJ, 592, 804
Lonsdale C. J., Farrah D., Smith H. E., 2006, Ultraluminous Infrared Galaxies, Springer/Praxis Books, Switzerland, p. 285
Malkan M. A., Jensen L. D., Rodriguez D. R., Spinoglio L., Rush B., 2017, ApJ, 846, 102
Martínez-Paredes M. et al., 2015, MNRAS, 454, 3577
Meijerink R., Spaans M., 2005, A&A, 436, 397
Meijerink R., Spaans M., Israel F. P., 2006, ApJ, 650, L103
Meijerink R., Spaans M., Israel F. P., 2007, A&A, 461, 793
Melnick J., Mirabel I. F., 1990, A&A, 231, L19
Nenkova M., Sirocky M. M., Ivezić Ž., Elitzur M., 2008a, ApJ, 685, 147
Nenkova M., Sirocky M. M., Nikutta R., Ivezić Ž., Elitzur M., 2008b, ApJ, 685, 160
Oda S., Tanimoto A., Ueda Y., Imanishi M., Terashima Y., Ricci C., 2017, ApJ, 835, 179
Privon G. C. et al., 2015, ApJ, 814, 39
Ptak A., Heckman T., Levenson N. A., Weaver K., Strickland D., 2003, ApJ, 592, 782
Ripple F., Heyer M. H., Gutermuth R., Snell R. L., Brunt C. M., 2013, MNRAS, 431, 1296
Saintonge A. et al., 2011a, MNRAS, 415, 32
Saintonge A. et al., 2011b, MNRAS, 415, 61
Saintonge A. et al., 2017, ApJS, 233, 22
Sanders D. B., Soifer B. T., Elias J. H., Madore B. F., Matthews K., Neugebauer G., Scoville N. Z., 1988, ApJ, 325, 74
Sanders D. B., Mazzarella J. M., Kim D.-C., Surace J. A., Soifer B. T., 2003, AJ, 126, 1607
Scoville N. Z., 1991, in Combes F., Casoli F., eds, Proc. IAU Symp. 146, Dynamics of Galaxies and Their Molecular Cloud Distributions. Kluwer, Dordrecht, p. 315
Scoville N. Z., 2013, in Falcon-Barroso J., Knapen J. H., eds, Evolution of Star Formation and Gas, Secular Evolution of Galaxies. Cambridge University Press, Cambridge, p. 491
Snell R. L., Narayanan G., Yun M. S., Heyer M., Chung A., Irvine W. M., Erickson N. R., Liu G., 2011, AJ, 141, 38
Soifer B. T. et al., 2000, AJ, 119, 509
Surace J. A., Sanders D. B., Vacca W. D., Veilleux S., Mazzarella J. M., 1998, ApJ, 492, 116
Treister E., Schawinski K., Urry C. M., Simmons B. D., 2012, ApJ, 758, L39
Veilleux S., 2012, in Iserlohe C., Karas V., Krips M., Eckart A., Britzen S., Fischer S., eds, Journal of Physics Conference Series, Vol. 372 , Germany, p. 012001
Veilleux S., Kim D.-C., Sanders D. B., Mazzarella J. M., Soifer B. T., 1995, ApJS, 98, 171
Veilleux S., Kim D. C., Sanders D. B., 2002, ApJS, 143, 315
Véron-Cetty M.-P., Véron P., 2010, A&A, 518, A10
Wild V. et al., 2011, MNRAS, 410, 1593
Wilson C. D. et al., 2008, ApJS, 178, 189
Wright E. L., 2006, PASP, 118, 1711
Young J. S., Scoville N. Z., 1991, ARA&A, 29, 581
Yuan T.-T., Kewley L. J., Sanders D. B., 2010, ApJ, 709, 884
Yun M. S., Carilli C. L., 2002, ApJ, 568, 88
Yun M. S. et al., 2015, MNRAS, 454, 3485

This paper has been typeset from a TEX/LATEX file prepared by the author.